Prototype of Kinetic Energy Storage System for Electrified Utility Vehicles in Urban Traffic

Johan Abrahamsson* Uppsala University Uppsala, Sweden

Magnus Hedlund Uppsala University Uppsala, Sweden

Hans Bernhoff Uppsala University Uppsala, Sweden

Abstract

This paper presents theoretical and experimental results on the ongoing construction of a high-speed (30 000 rpm) kinetic energy storage system (KESS). The purpose of the device is to function as a power buffer storing up to 1 kW h, primarily for utility vehicles in urban traffic. The KESS is connected in series between the primary power source and the traction motor of the vehicle. It comprises a composite rim of carbon and glass fiber in an epoxy matrix. The power to/from the rotating rim is transferred through an integrated double wound three-phase PM machine. The machine is levitated axially using four units with segmented Halbach arrays in a repulsive configuration. Radial centering is achieved through eight separate active electromagnetic actuators controlled by an FPGA. The geometries of the passive thrust units as well as the active actuators were designed using linked CAD and FEM tools controlled by advanced optimization algorithms. The simulated repulsive force from the thrust magnets was verified experimentally. Additionally, the corresponding negative stiffness in radial direction as well as the power loss due to induced eddy currents were simulated. The optimization of the active magnetic bearing (AMB) actuators resulted in a geometry with low resistive power loss, while generating a high current stiffness at the expense of maximum force.

1 Introduction

One of the main challenges in the electrification of the car fleet lies in the improvement of the electric power train. Although many of the presently available sources of energy used in electric vehicles have sufficiently high specific energy, their applicability is limited due to low specific power. It would therefore be of advantage to construct an electric driveline where the main energy storage is separated from the traction motor by a smaller power buffer [1].

Modern KESS fill a niche between super-capacitors with low specific energy but high specific power, and batteries with high specific energy but low specific power. The KESS has furthermore a long cycle-life, is not affected by changes in temperature or degrade over time. These properties make the KESS suitable for applications with high and frequent flows of energy, but where longterm storage is not vital. Buffering energy in electric vehicles has been identified as one promising application [2].

One of the first implementations of a flywheel for vehicular applications was as power buffer in the *Gyrobus*, first appearing in public in Switzerland in 1950. The steel flywheel in the Gyrobus had a weight of 1500 kg and a diameter of 1.6 m. The maximum rotational speed was 3000 rpm corresponding to a stored energy of around 24 MJ. Energy flux to and from the rotor was achieved through a three-phase asynchronous machine [3].

The flywheel concept was developed further during the second half of the 20:th century - notably by NASA, exploring the possibility of using it as energy storage in satellites. Genta published an excellent book on flywheels and in particular composite material in 1985 [4]. Post from the Lawrence Livermore published a sweeping article on the usage of high-speed flywheels in 1993 [5], among which also the usage as energy buffer in a vehicle was detailed.

*Contact Author Information: johan.abrahamsson@angstrom.uu.se, Box 534, 751 21 Uppsala Sweden, +46 18 471 5812

An implementation of the concept of the modern flywheel for vehicular applications with composite material and magnetic bearings was realized at the University of Austin, Texas in 1999 [6], [7]. The unit stored 7.2 MJ of energy and was able to deliver 150 kW of continuous power. Additionally, a theoretical investigation on the concept of low-speed flywheels for a bus was completed [8].

In 2007 the company *Flybrid Systems* developed a completely mechanical system for energy storage in vehicles called *KERS*, kinetic energy recovery system [9]. The unit was made specifically for the purpose of meeting the 2009 Formula One regulations. The KERS was capable of storing up to 400 kJ of usable energy at a rotational speed of 60 000 rpm, utilizing a 5 kg rotor. In 2011, Volvo Car Corporation announced their intention of building flywheel hybrid cars for mass production, basing their design largely on that of Flybrid Systems.

2 System Overview

The electric driveline under consideration in this project is based around a double wound synchronous electric machine attached to a flywheel. The primary energy source, the battery, is connected to the low power winding of the machine via an inverter. The energy from the high power winding of the machine undergoes controlled rectification in such a way that the DC-bus voltage is kept constant at a specified value. Finally, a second inverter is used to connect the DC-bus to the traction motor, see Figure 1.

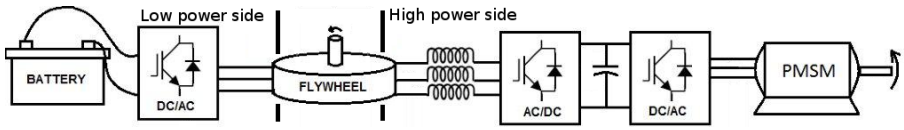

Figure 1: Overview of electric driveline. The double wound electric machine inside the flywheel separates the driveline in a low power side (LP) and a high power side (HP).

The double winding of the synchronous machine electrically insulates the battery from the traction motor. Additionally, it efficiently boosts the battery voltage by a fixed factor, which depends on the ratio of the number of turns in each of the two three-phase windings. In this way, the battery delivers a smooth power at relatively low voltage to the flywheel, while the flywheel feeds or receives pulsed power to/from the traction motor at a higher voltage level [10], [11].

3 Flywheel Overivew

A requirement for flywheels for vehicular applications is that they be lightweight and compact. The specific energy of a rotor can be written

$$k\frac{\sigma_\theta}{\rho}, \tag{1}$$

where k is a constant between 0 and 1 depending on geometry, σ_θ the ultimate tensile strength and ρ the mass density of the material. In order to maximize specific energy, a light and strong material should be chosen for the construction of the rotor. Presently, the material group which best fulfill these requirements are fiber-reinforced plastic, where the fibers may be made out of glass or carbon. Such rotors have reached values of specific energy of over $700\,\mathrm{kJ\,kg^{-1}}$ [12].

However, the very high rim-speed needed to begin to take advantage of the high tensile strength of these materials has certain implications on mechanical design. In particular, it leads to very high

rotational speed when space is limited. Operation in vacuum follows as a consequence since the drag losses grow with the power of 2.5 with rotational speed [13].

3.1 Prototype

The power transmission for the flywheel under construction is purely electrical, eliminating the need for a central shaft sticking out of the vacuum chamber. However, the combination of high rotational speed (30 000rpm) and enclosure in vacuum (400 Pa) suggested the usage of magnetic bearings in order to suspend the rotor, see Figure 2.

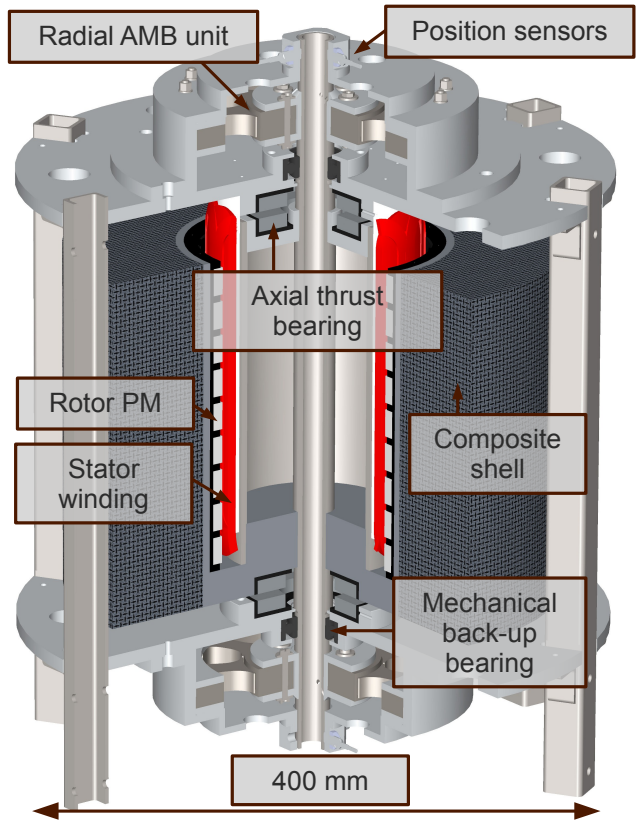

Figure 2: Overview of flywheel prototype under construction.

Passive thrust magnets in a cylindrical Halbach configuration were built in order to levitate the 40 kg heavy rotor axially. Eight actively controlled heteropolar electromagnetic actuators (AMB) were used to fixate the remaining four degrees of freedom.

The designed composite shell was 80 mm thick, and constructed from two layers of unidirectional composite material, an inner layer of glass-fiber surrounded by an outer layer of carbon-fiber. The radial pre-load required to reach the maximum rotational speed without delamination was achieved by altering the tension and material of the fiber during winding combined with shrink-fitting of the aluminum shell containing the rotor. In this way, the composite shell could be constructed in one single curing process.

3.2 Sensors

Four types of sensors were implemented into the electric machine

- Displacement sensors.

  Eddy-current sensors of type eddyNCDT 3010, S2 from the company Micro-Epsilon. The sensors have a measuring range of 2 mm, a linearity of 5 µm and a frequency response of 25 kHz. They were used to measure the position of the rotor, and deliver the input to the FPGA control of the AMB.

- Current sensors.

  0.1 Ω resistors from OHMITE coupled with Schottky diodes were used to achieve a bandwidth of 100 kHz and a resolution of 1 mA. The signal was amplified using an instrument amplifier PGA202KP from Teax Instruments. The current sensors were required to implement current control of the AMB and possibly enable sensorless control of the AMB.

- Temperature sensors.

  Both thermocouples from Labfacility (Z3-K-2M) as well as IR-thermopiles from GE Sensing (ZTP-135S) were implemented in order to monitor the temperature in the stationary parts as well as the rotating parts.

- Hall-effect sensors.

  Unipolar hall-effect sensors from Allegro (A1101) were inserted in the stator to provide information on the rotor position to the power electronic controlling the speed of the machine.

3.3 Electric machine

The electric machine integrated into the flywheel was a coreless, radial flux, permanent magnet machine with two separate sets of windings. The rotor magnets were placed on the inner surface of a thin cylindrical shell made of the aluminum alloy 7075, chosen for its high tensile strength and low mass density. The magnets were first mounted inside a plastic matrix, forming a cylindrical Halbach configuration in order to avoid the need for an outer magnetic back iron. An inner steel cylinder was used to close the flux path, increasing the magnetic field with approximately 15 %.

The concentrated stator windings were inserted between the two rotating cylinders. The windings of both the low- and high-power sides were three-pole, three-phase windings. A plot of the absolute value of magnetic field in a plane perpendicular to the axis of symmetry can be seen in Figure 3. The radial component of the magnetic field around the circumference of the motor at a radial position corresponding to the average radius of the stator windings, r_s was extracted from the simulation in order to evaluate the back-EMF. The magnitude of the fundamental component, $\hat{B}$, was found to amount to 0.18 T, see Figure 4.

The total magnetic flux, Φ_M, from the fundamental component through one turn of one pole of a phase-winding can be estimated as

$$\Phi_M(t) = h \int_{-\alpha/2}^{\alpha/2} \hat{B} \cos(3\varphi) r_s \mathrm{d}\varphi \cos(3\omega t) \tag{2}$$

where φ is mechanical angle, ω is the mechanical angular velocity of the rotor, α is the average angle spanned by the turn and h is the active height of the stator. Using Faraday's law of induction, the resulting phase-voltage, V_{ind}, of the complete winding of the machine can now be calculated as

$$V_{ind} = 6N\hat{B}\omega h r_s \sin\left(\frac{3\alpha}{2}\right) \sin(3\omega t), \tag{3}$$

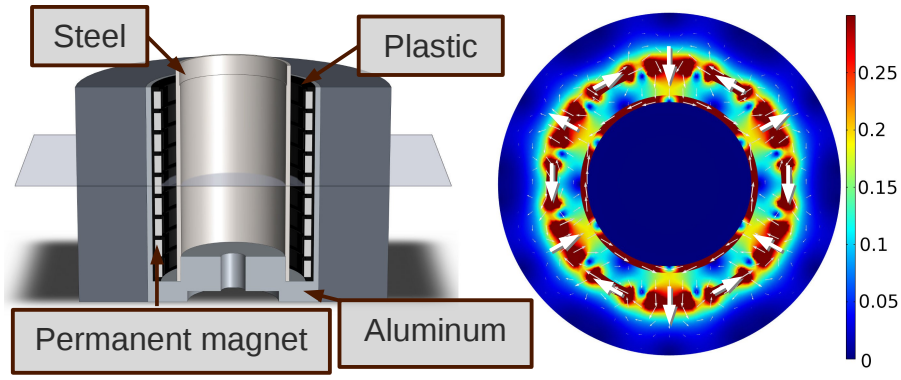

Figure 3: Magnetic field in the rotor of the electric machine. Left: CAD drawing of a axial cut of the rotor part. The transparent plane show the location of the simulation. Right: Simulation of the rotor magnetic field inside the electric machine. The color correspond to the absolute value of the B-field, and the white arrows mark its direction.

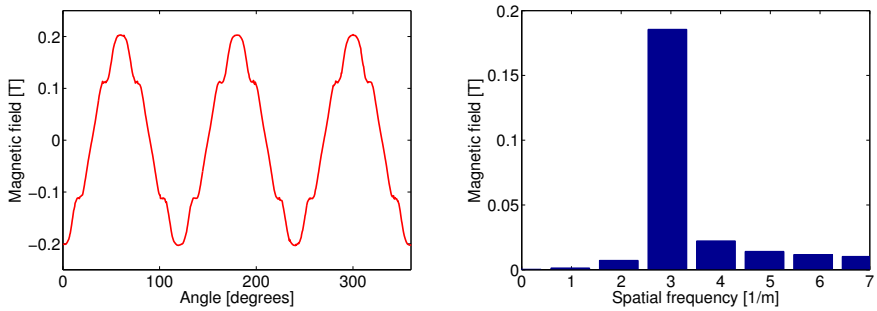

Figure 4: Analysis of the magnetic field of the rotor. Left: Evaluation of the radial B-field at the average radial position of the stator winding. Right: Fourier analysis of the average magnetic field, yielding a peak value of 0.18 T for the fundamental component.

where N is the number of turns of the winding. The parameters for the two sets of windings in the machine as well as RMS values for the calculated phase-voltages can be found in Table 1.

Parameter name	Low Power winding	High Power winding
α [deg]	32	30
h [mm]	220	220
r_s [mm]	74	72
$\hat{B}$ [Tesla]	0.18	0.18
N	4	10
ω [rpm]	30000	30000
V_{ind} (RMS) [V]	116	269

Table 1: Parameters and calculated values of RMS phase-voltage for the two sets of stator windings.

Note that the difference in RMS voltage between the high power side and the low power side can not be explained only by the quota of the number of turns in the windings. Additionally, the difference in the equivalent angle spanned by one turn as well as the radii at which the windings were placed had a significant impact on induced voltage.

4 Thrust bearing

The axial degree of freedom of the rotor was passively balanced using two sets of permanent magnetic arrays mounted on either end of the shaft. Each unit consisted of grade N42 NdFeB-magnets mounted in two circular symmetric halbach arrays, see Figure 5 for one such set.

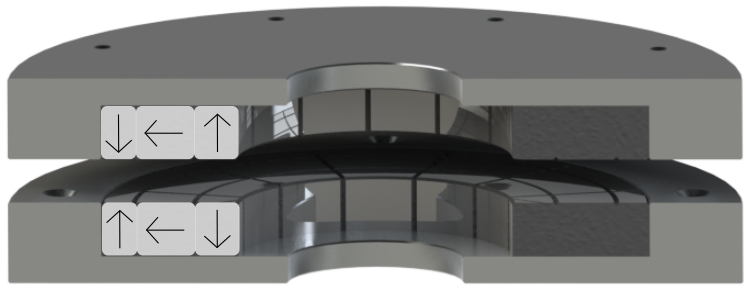

Figure 5: Definition of the direction of the individual permanent magnets in the Halbach unit. The magnets were made of NdFeB of grade N42.

The radial dimensions of the individual magnets were optimized in a two-dimensional axisymmetric model. The optimizing variable was thrust force. By keeping the outer and inner radial dimensions fixed at 25 mm and 50 mm respectively, the optimizer worked in a two dimensional room. The height of the magnets were 10 mm. The resulting configuration can be found in Table 2.

Magnet position	Inner radius [mm]	Outer radius [mm]
Inner Magnet	25	33
Middle Magnet	33	44
Outer Magnet	44	50

Table 2: Optimized Halbach geometry

The assembly of the thrust bearing was facilitated by the construction of an auxiliary tool for mounting triplets of permanent magnets. Each triplet consisted of one segment of the complete unit. The contacting surfaces of the three magnets were roughened with abrasive paper, cleaned and placed in a semi-stable configuration with the middle magnet vertically displaced. Afterwards, the complete configuration was placed in the mounting tool, forced into place and glued, see Figure 6.

Finally, the triplets were glued to the bottom of a plastic cup and to each other. An aluminum flange was shrink-fitted to the plastic cup by heating it to 175 °C and pressing the two parts together, see Figure 7.

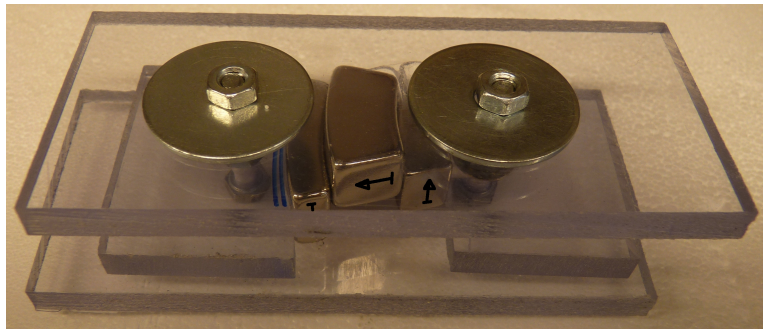

Figure 6: Assembly of the magnetic triplets in a Halbach array. The assembly tool was made from 6 mm thick plexiglas.

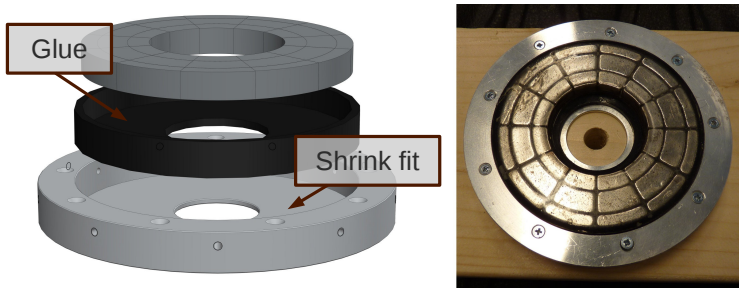

Figure 7: Construction of one Halbach array. The magnets were glued to each other and to a plastic cup using Loctite 496. Further, an aluminum holder was shrink-fitted onto the cup by heating it to 175 °C. A CAD drawing describing the assembly process can be seen to the left. The finished unit can be seen on the right.

4.1 Lift Force Evaluation

Note that the optimizer operated in a 2D axisymmetric space. The magnets were in reality segmented circumferentially into 12 pieces in order to facilitate production and decrease mechanical stress during rotation. To more accurately calculate the resulting lift force, a smaller segment of the array was analyzed in greater detail.

The lift force between two Halbach arrays was measured empirically as well as simulated using FEM. The measurements were acquired by mounting the assembled arrays in a wooden structure with a moving centerpiece pushing down on two scales, see Figure 8. The top bar contained the upper part of the thrust bearing, and was forced down by nuts attached to threaded rods.

Corresponding simulations were performed by modeling a 30° segment of one bearing set, in order to achieve maximum resolution in the area between magnets. Periodic boundary conditions were used to attain symmetry properties, thus emulating a 360-degree simulation. Measured datapoints from three separate tests as well as the results of the simulation can be found in Figure 9.

Evaluation of the axial stiffness of the simulated values yielded a value of $272\,\mathrm{N\,mm^{-1}}$ at the nominal air-gap of 5 mm. Given that two such systems was used (one at the top, and one at the bottom) the total stiffness in axial direction at the nominal position was estimated to $544\,\mathrm{N\,mm^{-1}}$. A resulting axial equilibrium point located 0.75 mm below the nominal value could therefore be found due to the weight of the rotor (approximately 40 kg), when placing the machine vertically.

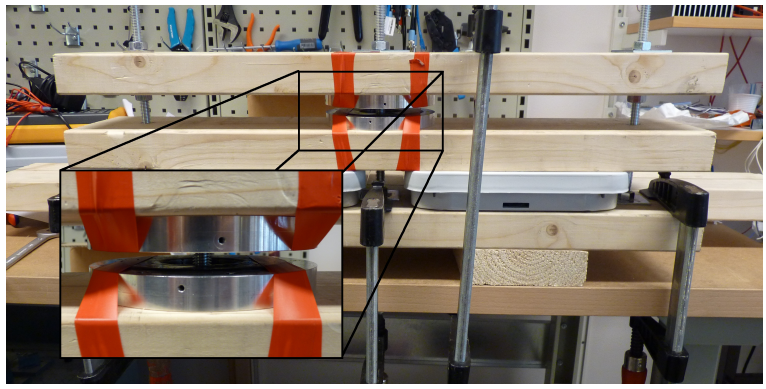

Figure 8: Measurements of the liftforce of a pair of Halbach arrays. An axial stiffness of $272\,\mathrm{N\,mm^{-1}}$ was calculated at the nominal air-gap of 5 mm.

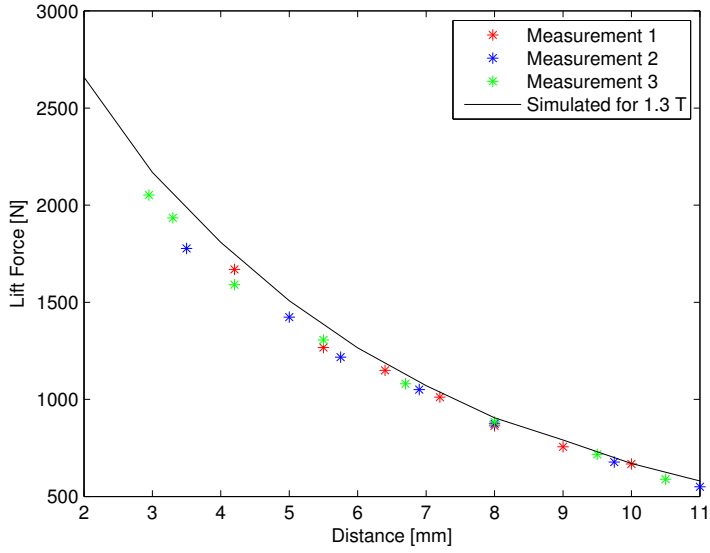

Figure 9: Measurements of the liftforce of a pair of Halbach units were performed and compared with simulated values. Good correspondence was found between the simulated and measured values.

4.2 Radial Stiffness

As shown by Earnshaw's theorem, and in particular with the extension of Braunbek [14], a system built solely of permanent magnets is naturally unstable. Consider a stationary magnetic dipole, situated in an external magnetic field, with no free currents. The corresponding magnetic potential energy, U_M, becomes

$$U_M = \vec{m} \cdot \vec{B}, \tag{4}$$

where $\bar{m}$ is the magnetic dipole moment and $\bar{B}$ the external magnetic field. It is not difficult to find a configuration with $\vec{\nabla} U_M = \vec{0}$, implying that the resulting force on the dipole from the external

magnetic field is zero in all directions. However, from the Maxwell equations

$$\begin{cases} \vec{\nabla} \cdot \vec{B} = 0 \\ \vec{\nabla} \times \vec{B} = 0 \end{cases} \tag{5}$$

it follows that the Laplacian of each individual component of $\vec{B}$ must be zero

$$\nabla^2 B_x = \nabla^2 B_y = \nabla^2 B_z = 0. \tag{6}$$

From this, it is clear that $\nabla^2 U_M = 0$ implying that at all possible critical points in the volume under consideration must be saddle points. The same reasoning can be applied to show that para- and ferromagnetic materials are naturally unstable, while diamagnetic materials may be stably levitated.

The generation of positive axial stiffness, K_a, using permanent magnets thereby causes a negative radial stiffness, K_r. The magnitude of the corresponding negative radial stiffness can be found to be [15]

$$K_a + 2K_r \leq 0. \tag{7}$$

The radial stiffness for the Halbach structure was evaluated using FEM-software, using an unsegmented geometry with nominal radial magnetization. The radial stiffness at the nominal air-gap was found to be in the range of $-120\,\mathrm{N\,mm^{-1}}$ to $-160\,\mathrm{N\,mm^{-1}}$, which can be compared with the previously measured axial stiffness of $272\,\mathrm{N\,mm^{-1}}$.

4.3 Losses

Due to the tolerance in the magnitude of the remanence, as well as the discretization of magnetizing direction due to segmentation of the magnetic rings, the rotating magnets will expose the system to a time-varying magnetic field. This magnetic field will further induce a voltage, generating eddy-currents in the conductive materials.

A FEM-model was used in a similar setup as mentioned above, with an added velocity (Lorentz) term in the domains affected by the eddy currents

$$\nabla \times \bar{H} - \sigma \bar{v} \times \bar{B} = \bar{J}. \tag{8}$$

The system was then simulated in its stationary state. A graph of bearing losses for one single bearing set at the highest rated speed of 30 000 rpm is shown in Figure 10. The conductivity of NdFeB was set to $1.4 \times 10^7\,\mathrm{S\,m^{-1}}$ and to $3.5 \times 10^7\,\mathrm{S\,m^{-1}}$ for aluminum. Note that the losses increase with decreased airgap (increased load). Thus, axial bearing efficiency can be optimized by operating in a lower stiffness region.

The power loss due to eddy currents at the estimated equilibrium position (0.5 mm below the nominal position) was found to amount to 23 W per Halbach segment. Assuming that this heat rapidly becomes evenly distributed over the magnetic material, the heat transfer over the plastic cup separating the magnets from the aluminum flange can be calculated by

$$J = \kappa \frac{S \Delta T}{\Delta x}, \tag{9}$$

where J is the amount of heat passing the plastic cup per unit of time, κ the thermal conductivity, S the area of the cup, ΔT the relative temperature between magnets and flange and Δx the thickness of the plastic material. Using values of $9 \times 10^{-3}\,\mathrm{m^2}$ for the total surface area (bottom plate plus sides of the magnets), a thickness of 5 mm and a thermal conductivity of $0.25\,\mathrm{W\,m^{-1}\,K^{-1}}$ yields a

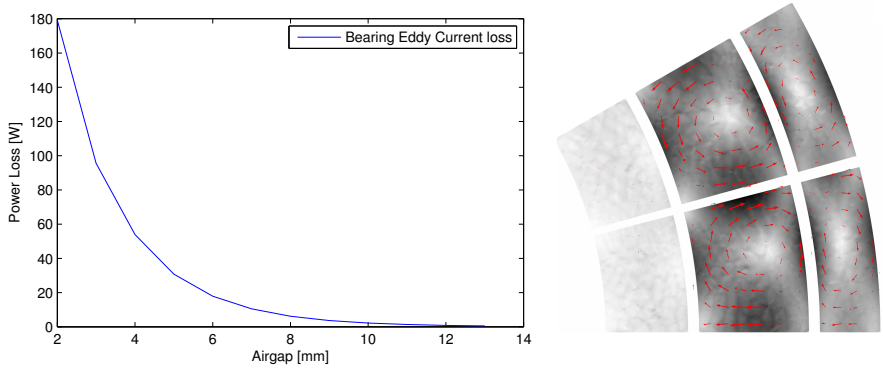

Figure 10: FEM simulation of eddy current loss in the permanent magnets as function of the air-gap between the Halbach arrays. To the left, the power loss as function of airgap at 30 000 rpm. To the right, a qualitative image of the magnitude and direction of the induced eddy currents.

required temperature difference of 51 K. This temperature difference was found to be acceptable, assuming an ambient temperature of 25 °C.

Air friction due to drag was not considered, since the system was assumed to operate in vacuum. Also hysteresis losses were neglected since all material in the vicinity of the permanent magnets, as well as the magnets themselves, had permeability very close to unity.

5 Radial bearing

The four remaining degrees-of-freedom of the system were stabilized by two sets of four actively controlled electromagnetic actuators in differential operation. The actuators were constructed using non-oriented laminated electro-steel from Surahammars Bruk. The rotating target of the unit was constructed using 100 pieces of 0.2 mm thick steel plate. The corresponding stator was constructed using 24 pieces of 0.65 mm thick steel plate, see Figure 11.

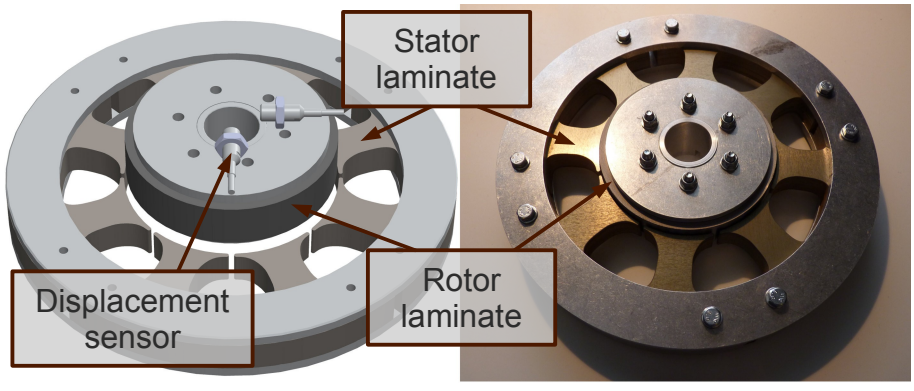

Figure 11: Overview of four of the eight electromagnetic actuators and the rotor target. The rotor stack consisted of 100 pieces of 0.2 mm thick non-oriented electro-steel. The stator stack comprised 24 pieces of 0.65 mm thick non-oriented electro-steel.

The plates were water-cut from 3D CAD drawings and assembled, after which the area of the air-gap was further processed in a lathe in order to reach the defined tolerance, a radial airgap of 1 mm. Water-cutting is reported to have a smaller impact on the magnetic properties of the steel than punching or laser cutting, [16]. Additionally, any geometrical shape (including splines) could be realized without limitations on radii of curvature.

5.1 Geometrical optimization

Considering the very poor cooling capability of an electromagnet enclosed in vacuum, a quite low effective current density of $1\,\mathrm{A\,mm^{-2}}$ was set as limit for the generation of bias current. The exact shape of the stator laminate had to be defined. The more narrow the legs of the electromagnet, the more space available for the windings. However, this would also lead to a higher degree of saturation in the stator, and higher total resistive loss in the windings. The optimization criteria chosen was to maximize the attractive force of the actuator over total resistive loss in the windings, given the current density.

To this end the geometry of the laminate was parametrized in SolidWorks, using the radial and circumferential position of five points, connected with splines. A direct coupling between SolidWorks and Comsol was used to solve for the attractive force between stator and rotor numerically. The *Genetic Algorithm* routine of the Matlab Global Optimization Toolbox was further used to update the positions of the spline points. A similar approach can be found in [17]. The resulting geometry was compared with a reference geometry consisting of a leg where the area of the cross-section was kept constant, see Figure 12.

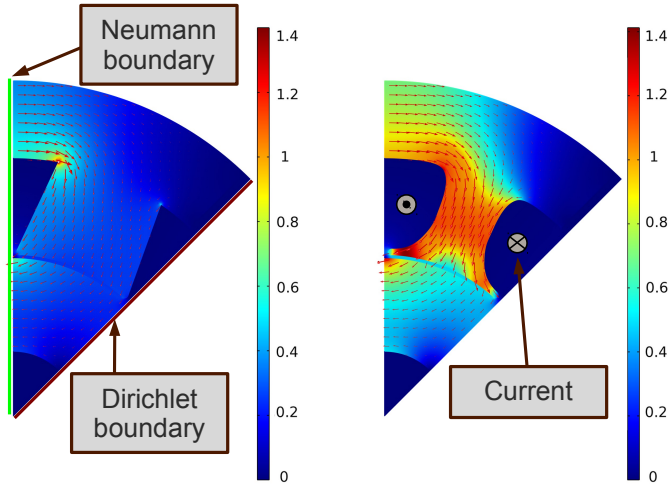

Figure 12: Comparison between a laminated actuator with a geometry based on constant flux area (left) and one optimized for maximum force over loss ratio given a specific current density (right). An effective current density of $1\,\mathrm{A\,mm^{-2}}$ was used.

The optimized geometry generated a magnetic bias field of 0.5 T in the airgap between stator and rotor for an applied current density of $1\,\mathrm{A\,mm^{-2}}$, compared with 0.25 T for the geometry with constant cross section. Furthermore, simulations showed that a current density of $2\,\mathrm{A\,mm^{-2}}$ was required in order to reach the same magnetic bias field in the geometry with constant cross-section. This can be understood since the reluctance in the magnetic path was dominated by the airgap.

However, since the area of the cross-section of the winding in the optimized geometry was twice that in the geometry with constant cross-section, the total resistive loss for the same bias field became half.

Furthermore, the current stiffness for a system of two optimized actuators operating in differential mode was studied, see 13. It was found that the maximum current stiffness occurred at the oper-

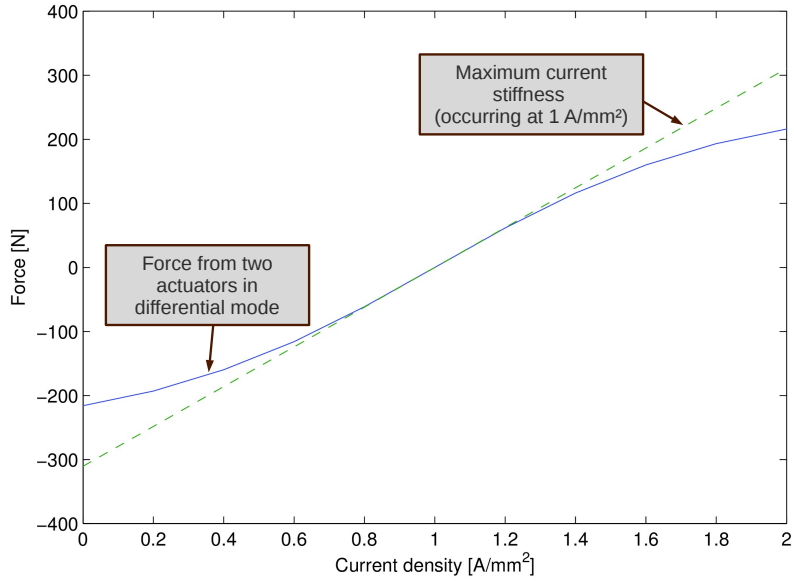

Figure 13: Evaluation of resulting force from two actuators in differential mode. The maximum current stiffness amounted to $310.5\,\mathrm{N/(A/mm^2)}$ and occurred at $1\,\mathrm{A\,mm^{-2}}$, the operating point.

ating point of current density used in the geometrical optimization. Its maximum value amounted to $310.5\,\mathrm{N/(A/mm^2)}$. The current stiffness was further found to exhibit good linearity around this operating point, between $0.7\,\mathrm{A\,mm^{-2}}$ to $1.3\,\mathrm{A\,mm^{-2}}$. However, outside this range the deviation from a quadratic relationship between current and force due to saturation of the laminate caused large deviations from linearity. This also resulted in a limitation of maximum achievable force to 216 N.

The corresponding value of current stiffness generated by the constant cross-section geometry was $374\,\mathrm{N/(A/mm^2)}$. The optimized geometry thereby reached a 83 % of the current stiffness, while incurring only 50 % of the resistive loss.

6 Summary

A high-speed (30 000 rpm) electric machine reinforced with a composite material rim, primarily for usage as energy buffer in an electric utility vehicle in urban traffic, has been designed and is under construction. The prototype utilizes a coreless double-wound PM synchronous machine for power transmission, and is designed to operate in vacuum.

The composite material rim was constructed using an inner layer of glass fiber reinforced epoxy and an outer layer of carbon fiber reinforced epoxy. The rim was wound unidirectional with varying preload, and cured in one piece.

Axial levitation of the rotor was achieved by four cylindrical Halbach arrays, capable of generating an axial stiffness of $544\,\mathrm{N\,mm^{-1}}$ at the nominal position. Measurements of axial force was compared with simulations and good agreement was found. Simulations were further performed on the steady state losses in the thrust bearings.

Radial stabilization was generated through eight actively controlled electromagnets. The geometry of the actuators were optimized using a combination of SolidWorks, Comsol and Matlab in such a way that 83 % of the current stiffness was achieved while generating only 50 % resistive loss. However, saturation of the electric steel lead to a decrease of maximum force from 374 N to 216 N.

References

[1] J. Abrahamsson, J. de Santiago, J.G. Oliveira, J. Lundin, and H. Bernhoff. Prototype of electric driveline with magnetically levitated double wound motor. In *Electrical Machines (ICEM), 2010 XIX International Conference on*, 2010.

[2] Björn Bolund, Hans Bernhoff, and Mats Leijon. Flywheel energy and power storage systems. *Renewable and Sustainable Energy Reviews*, 11(2):235 – 258, 2007.

[3] The oerlikon electrogyro. Technical report, Automobile Engineer, 1955.

[4] Giancarlo Genta. *Kinetic Energy Storage: Theory and Practice of Advanced Flywheel Systems*. Butterworth-Heinemann Ltd, London, 1985.

[5] R.F. Post, T.K. Fowler, and S.F. Post. A high-efficiency electromechanical battery. *Proceedings of the IEEE*, 81(3):462 –474, mar 1993.

[6] M. M. Flynn, J. J. Zierer, and R. C. Thompson. Performance testing of a vehicular flywheel energy system. In *Proceedings of the SAE World Congress & Exhibition*, 2005.

[7] R.J. Hayes, J.P. Kajs, R.C. Thompson, and J.H. Beno. Design and testing of a flywheel battery for a transit bus. Technical report, Society of Automotive Engineers, SAE, 1999.

[8] C.S. Hearn, M.M. Flynn, M.C. Lewis, R.C. Thompson, B.T. Murphy, and R.G. Longoria. Low cost flywheel energy storage for a fuel cell powered transit bus. In *Vehicle Power and Propulsion Conference, 2007. VPPC 2007. IEEE*, pages 829 –836, sept. 2007.

[9] D. Cross and J. Hilton. High speed flywheel based hybrid systems for low carbon vehicles. In *Hybrid and Eco-Friendly Vehicle Conference, 2008. IET HEVC 2008*, pages 1 –5, dec. 2008.

[10] J. G. Oliveira, J. Abrahamsson, and H. Bernhoff. Battery discharging power control in a double-wound flywheel system applied to electric vehicles. *International Journal of Emerging Electric Power Systems*, 12(1):235–258, 2011.

[11] J. G. Oliveira. *Power Control Systems in a Flywheel based All-Electric Driveline*. PhD thesis, Division for electricity, Uppsala University, Sweden, 2011.

[12] K. Takahashi, S. Kitade, and H. Morita. Development of high speed composite flywheel rotors for energy storage systems. *Advanced Composite Materials*, 11:40–49, 2002.

[13] Juha Saari. *Thermal analysis of high-speed induction machines*. PhD thesis, Espoo, 1998. Diss. Espoo : Tekn. korkeak.

[14] Werner Braunbek. Freischwebende körper im elektrischen und magnetischen feld. *Zeitschrift für Physik A Hadrons and Nuclei*, 112:753–763, 1939. 10.1007/BF01339979.

[15] A. Filatov and E. Maslen. Passive magnetic bearing for flywheel energy storage systems. *IEEE Transactions on Magnetics*, 37:3913–3924, 2001.

[16] A Schoppa, H Louis, F Pude, and Ch von Rad. Influence of abrasive waterjet cutting on the magnetic properties of non-oriented electrical steels. *Journal of Magnetism and Magnetic Materials*, 254–255(0):370 – 372, 2003. Proceedings of the 15th International Conference on Soft Magnetic Materials (SMM15).

[17] Adam Pilat. Analytical modeling of active magnetic bearing geometry. *Applied Mathematical Modelling*, 34(12):3805 – 3816, 2010.